

Pressure tuning of competing magnetic interactions in intermetallic CeFe₂

Jiyang Wang,¹ Yejun Feng,^{1,2,*} R. Jaramillo,³ Jasper van Wezel,⁴
P. C. Canfield,⁵ and T. F. Rosenbaum¹

¹*The James Franck Institute and Department of Physics, The University of Chicago, Chicago, Illinois 60637, USA*

²*The Advanced Photon Source, Argonne National Laboratory, Argonne, Illinois 60439, USA*

³*School of Engineering and Applied Sciences, Harvard University, Cambridge, Massachusetts 01238, USA*

⁴*Materials Science Division, Argonne National Laboratory, Argonne, Illinois 60439, USA*

⁵*Ames Laboratory and Department of Physics and Astronomy, Iowa State University, Ames, Iowa 50011, USA*

(Received 1 May 2012; published 20 July 2012)

We use high-pressure magnetic x-ray diffraction and numerical simulation to determine the low-temperature magnetic phase diagram of stoichiometric CeFe₂. Near 1.5 GPa we find a transition from ferromagnetism to antiferromagnetism, accompanied by a rhombohedral distortion of the cubic Laves crystal lattice. By comparing pressure and chemical substitution we find that the phase transition is controlled by a shift of magnetic frustration from the Ce-Ce to the Fe-Fe sublattice. Notably the dominant Ce-Fe magnetic interaction, which sets the temperature scale for the onset of long-range order, remains satisfied throughout the phase diagram but does not determine the magnetic ground state. Our results illustrate the complexity of a system with multiple competing magnetic energy scales and lead to a general model for magnetism in cubic Laves phase intermetallic compounds.

DOI: [10.1103/PhysRevB.86.014422](https://doi.org/10.1103/PhysRevB.86.014422)

PACS number(s): 75.30.Kz, 75.50.Ee, 75.20.En, 75.10.Jm

I. INTRODUCTION

Many materials exhibit multiple magnetic interactions with a broad range of interaction energies. In such cases the crystal lattice typically prohibits the formation of an ordered state in which the magnetic interaction energies of all possible pairs of ions are simultaneously minimized, and the system often has to “choose” among competing configurations, with each carrying a different amount of frustration. If the dominant interaction is geometrically frustrated, this competition may even result in a disordered magnetic ground state with no long-range order. Prominent examples include spin glasses made of randomly separated magnetic ions,¹ and spin ices or liquids on geometrically constrained two-dimensional kagome and three-dimensional pyrochlore lattices.^{2–4}

Even if the major interaction is satisfied and long-range order is established, frustration can still play a role in determining the magnetic ground state, due to competition between weaker magnetic interactions. A well-known example is that of Heisenberg spins on a square lattice with antiferromagnetic nearest-neighbor and next-nearest-neighbor interactions. In this case, the magnetic order depends on the relative strength of the two magnetic interactions, which can be tuned through a sequence of quantum phase transitions.⁵ Likewise, in the pyrochlore oxides Gd₂Sn₂O₇ and Gd₂Ti₂O₇ the balance between second and third nearest-neighbor interactions is responsible for the emergence of multiple antiferromagnetic phases with varying magnetic wave vectors.⁶ From a conceptual standpoint, geometrical frustration of secondary interactions (i.e., magnetic interactions much weaker than the primary interaction) is interesting because ostensibly minor phenomena can play an outsized role in determining the magnetic ground state. Identifying frustration and competition among weaker degrees of freedom may then provide a vantage point for studying the complex magnetic behavior of interesting and potentially useful magnetic materials with nontrivial magnetic phase diagrams.

Here we focus on the rare-earth intermetallic ferromagnet CeFe₂,^{7–11} which is a metallic compound with cubic Laves crystal symmetry, and is related to a broader class of pyrochlore lattice systems.² The Fe ions are located on a pyrochlore sublattice of corner-sharing tetrahedra, which can be viewed as a collection of alternating, two-dimensional kagome and triangular lattice planes stacked along the $\langle 111 \rangle$ direction.² The triangular Fe lattices are woven through by Ce ions in a corrugated manner. In Fig. 1 we show a perspective stretched along the $\langle 111 \rangle$ direction for clarity.

Many metallic cubic Laves systems exhibit either ferromagnetic or antiferromagnetic long-range order.^{7–14} Ferromagnetic CeFe₂ is close to a magnetic instability and can be switched to an antiferromagnet with either chemical doping or applied pressure. In this work we quantitatively demonstrate how the competition between two secondary magnetic interactions determines the magnetic phase diagram of CeFe₂. The primary magnetic interaction, which sets the temperature scale for the onset of long-range order, remains satisfied throughout the phase diagram. However, this is not sufficient to determine the magnetic ground state. The ferromagnetic-antiferromagnetic transition is instead driven by the transfer of frustration between two sets of secondary magnetic interactions.

II. GENERIC PHASE DIAGRAM FOR CeFe₂

There exists extensive literature on chemically doped CeFe₂, with numerous choices of dopants replacing either Ce, or Fe, or both.^{15–22} The ferromagnetic ground state of CeFe₂ undergoes a phase transition to an antiferromagnet with small amounts of chemical doping on the Fe site by one of many elements including Al, Co, Ru and Ir.^{15–22} Previous work on stoichiometric CeFe₂ found evidence for a new phase at high pressure which, by comparison with the doped systems, was suggested to be the antiferromagnetic phase.^{23–25} The proximity of stoichiometric CeFe₂ to an antiferromagnetic

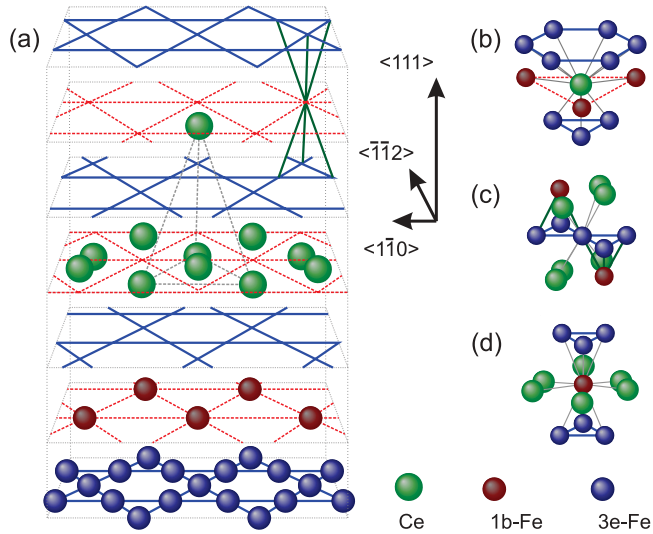


FIG. 1. (Color online) (a) Perspective of the cubic Laves lattice of CeFe_2 , emphasizing the layered structure and elongated along the $\langle 111 \rangle$ axis for clarity. The structure consists of stacked sheets of $3e$ -Fe sites in a kagome lattice, alternating with corrugated sheets of Ce sites and $1b$ -Fe sites in a triangular lattice. Not all atoms are shown for the sake of clarity. Solid lines indicate the nearest-neighbor pairing and dashed lines indicate next-nearest-neighbor pairing. (b)–(d) Clusters of twelve nearest neighbors are shown surrounding each type of atomic site.

instability is also supported by the observation of antiferromagnetic fluctuations within the ferromagnetic phase.^{9,10,24}

It is useful to compare the phase diagram of CeFe_2 under pressure to the results of doping with Al, Co, Ru, and Ir. We choose specifically these dopants because they preserve the cubic Laves structure when fully replacing Fe in CeFe_2 .²⁶ Phase diagrams were collected from the literature for CeFe_2 under pressure,^{22,23,25} $\text{Ce}(\text{Fe}_{1-x}\text{Co}_x)_2$ at both ambient (up to 16%)^{17,22,25} and high pressure (for 5, 7, and 10%),^{22,25} $\text{Ce}(\text{Fe}_{1-x}\text{Al}_x)_2$ (up to 15%),¹⁶ $\text{Ce}(\text{Fe}_{1-x}\text{Ru}_x)_2$ (up to 15%),¹⁸ and $\text{Ce}(\text{Fe}_{1-x}\text{Ir}_x)_2$ (up to 8%).²⁰ The lattice constants are interpolated from published data for $\text{Ce}(\text{Fe}_{1-x}\text{Co}_x)_2$,²¹ $\text{Ce}(\text{Fe}_{1-x}\text{Al}_x)_2$,¹⁵ and $\text{Ce}(\text{Fe}_{1-x}\text{Ru}_x)_2$.¹⁸ No lattice constant data for $\text{Ce}(\text{Fe}_{1-x}\text{Ir}_x)_2$ is available so we used Vegard's law to interpolate between CeFe_2 and CeIr_2 .²⁷ Lattice constants of CeFe_2 under pressure were taken from our own results. We also assume that the low-temperature compressibility of $\text{Ce}(\text{Fe}_{1-x}\text{Co}_x)_2$ is the same as our measured value for CeFe_2 .

The compiled phase diagrams are plotted in Fig. 2(a). We note that although the antiferromagnetic state is consistently reached with chemical doping or applied pressure, the lattice constant does not vary uniformly with these tuning parameters. Applying pressure and doping with Co compresses the lattice, while doping with Al, Ru, or Ir expands the lattice. The apparent insensitivity of the ferromagnetic-antiferromagnetic phase transition to the lattice spacing shows that the doping phase diagram is not controlled by “chemical pressure,” whereby the effect of chemical substitution is merely to expand or contract the lattice. Rather, we show in Fig. 2(b) that the pressure and doping phase diagrams can be collapsed into a single generic phase diagram using a tuning parameter η , which is a linear combination of pressure P (in GPa) and

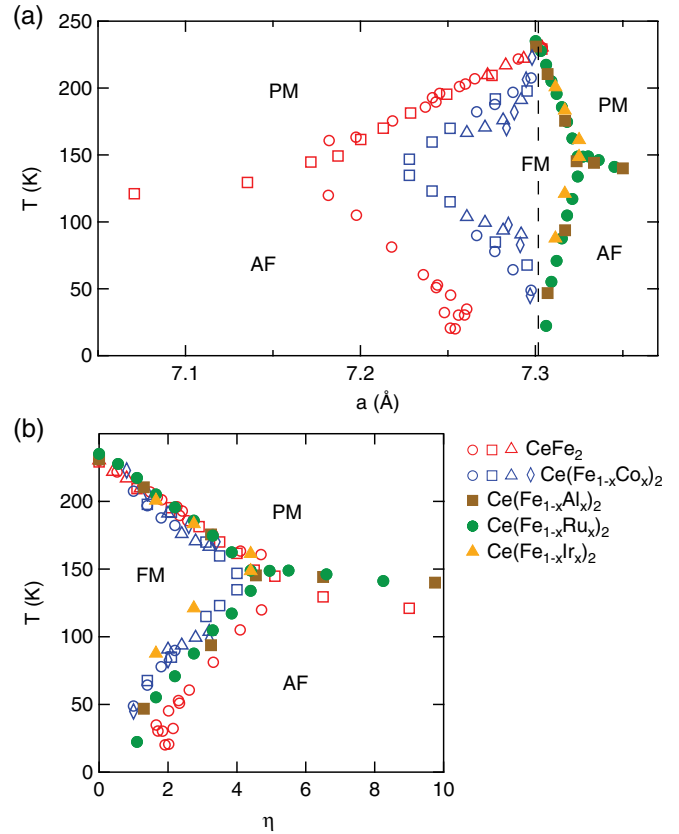


FIG. 2. (Color online) (a) Compilation of published data on the magnetic phase behavior of stoichiometric and chemically doped CeFe_2 . Magnetic transition temperatures are plotted as a function of lattice constant a . The paramagnetic (PM), ferromagnetic (FM), and antiferromagnetic (AF) phases are indicated. The AF phase can be reached with both decreasing and increasing lattice constant. (b) A generic phase diagram for CeFe_2 is created by collapsing the phase diagrams shown in (a) using a tuning parameter η , which is a linear combination of pressure P (in GPa) and doping x (in %) according to $\eta = P + Ax$. A is a positive, dopant-specific scaling factor with $A = 0.20, 0.65, 0.55,$ and 0.55 GPa/% for Co, Al, Ru, and Ir, respectively.

doping x (in %): $\eta = P + Ax$. Here A is a numerical factor that is specific to the individual dopant and is always positive. Importantly, the effective parameter η scales the horizontal axis but not the temperature axis. The collapse of the phase diagrams, and in particular the multicritical point between the paramagnetic, ferromagnetic, and antiferromagnetic phases around 150 K, suggests that there is a primary magnetic energy scale which determines the critical temperature for the onset of long-range order. This energy scale is independent of the tuning parameter η that determines the type of magnetic ground state. What Fig. 2(a) implies is that η should not have a simple, monotonic dependence on lattice, and thus is unlikely to be due to a single energy scale.

III. EXPERIMENTAL METHODS

Single crystals of CeFe_2 were grown from a Ce-rich binary melt with initial composition $\text{Ce}_{0.6}\text{Fe}_{0.4}$. High purity Ce (Ames Lab) and Fe were sealed into a three-cap Ta crucible²⁸ and subsequently sealed into a silica ampule. The ampule was

heated from room temperature to 1100 °C over 6 hours, cooled to 950 °C over 3 hours and then slowly cooled to 700 °C over 120 hours. Once at 700 °C the excess liquid was decanted from the single crystals.²⁸

With sensitivity to both lattice and magnetic symmetry, and compatibility with high-pressure diamond anvil cells, synchrotron x-ray diffraction is well suited for studying the pressure-temperature phase diagram of an antiferromagnet.^{29,30} X-ray diffraction measurements were performed at beamline 4-ID-D of the Advanced Photon Source. A double-bounce Si (111) monochromator and a pair of palladium (with a K edge at 24.35 keV) coated mirrors produced a focused beam of 20 keV x rays free from contamination by higher harmonics. CeFe₂ crystals of typical dimensions 70 × 70 × 40 μm³ were loaded in the diamond anvil cell in an argon atmosphere to avoid oxidation. The pressure medium was a 4:1 (volume) methanol:ethanol mixture. A polycrystalline silver grain was used as an *in situ* manometer.³⁰ A helium-membrane-tuned diamond anvil cell was used to continuously vary pressure at the cryostat base temperature of 3.5 K. Nonresonant x-ray magnetic diffraction was carried out in the transmission geometry and within the vertical scattering plane for high momentum space resolution. The use of 70° full cone Boehler-Almax diamond anvils allowed access to a wide range of reciprocal space. A total of four samples were studied under pressure at $T = 3.5$ K. The FWHM of the sample mosaic curve never exceeded 0.10° under pressure. The possibility of contamination by second harmonic x rays was ruled out by monitoring a secondary detection channel set to count 40 keV x rays on the NaI scintillation detector. The null signal on this secondary channel and the extremely low intensity of the observed (1/2, 1/2, 1/2)-type peaks (Fig. 4) rule out the charge scattering contribution to the measured magnetic diffraction peaks.

IV. DIRECT MEASUREMENTS OF LATTICE SYMMETRY AND ANTIFERROMAGNETISM UNDER PRESSURE

We plot in Fig. 3 the response of the crystal lattice to applied pressure, P , at low temperature. Near $P = 1.5$ GPa the lattice undergoes a transition from cubic to rhombohedral symmetry. The rhombohedral distortion is a compression along one of the four cubic body diagonals, and splits the cubic crystal into four types of rhombohedral crystal domains. Using high-resolution x-ray diffraction it is possible to index diffraction peaks by their rhombohedral domain type. The compressibility B_0 is determined by fitting the lattice constant $a(P)$ to a one-parameter Birch equation³⁰ with $B_0 = 90 \pm 4$ GPa and 105 ± 5 GPa in the low- and high-pressure phases, respectively. In the high-pressure phase the unit cell angle α deviates from 90° by $0.327^\circ \pm 0.002^\circ$. The data also show clear evidence for a regime of phase coexistence between 1.3 and 1.8 GPa. The presence of a structural phase transition and a regime of phase coexistence are consistent with magnetic susceptibility studies of CeFe₂ under pressure, which found the ferromagnetic phase boundary to be difficult to pin down at low temperature.²⁵ Note also that a rhombohedral distortion is known to accompany the ferromagnetic-to-antiferromagnetic phase transition in Ru-, Al-, and Co-doped CeFe₂, with α in the range 90.2°–90.31°.¹⁹ The discovery that stoichiometric CeFe₂ experiences a similar

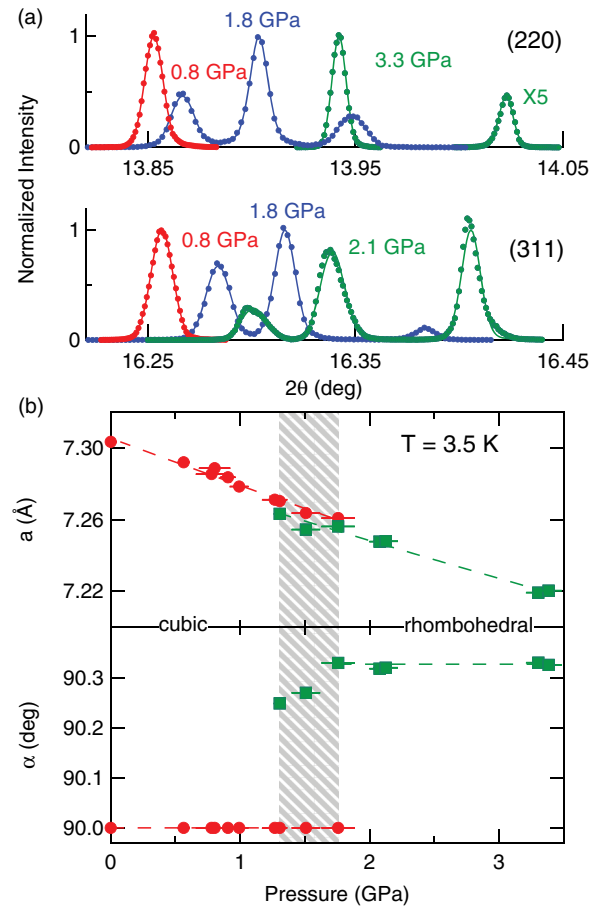


FIG. 3. (Color online) Evolution of the CeFe₂ crystal lattice with pressure at $T = 3.5$ K. (a) Longitudinal ($\theta - 2\theta$) scans of the (2, 2, 0) and (3, 1, 1) Bragg peaks at three pressures: in the low-pressure cubic phase, in the regime of phase coexistence, and in the high-pressure rhombohedral phase. The peak splitting at high pressure is evidence of the rhombohedral distortion. The splitting of the (2, 2, 0) peak at $P = 1.8$ GPa indicates a regime of phase coexistence; for the (3, 1, 1) reflection at 1.8 GPa the peak from the cubic phase is indistinguishable from the rhombohedral (3, 1, -1) peak within our measurement resolution (we follow the convention that the rhombohedral distortion compresses the $\langle 111 \rangle$ axis). (b) Dependence of the lattice constant a and the cell-axis angle α on pressure. The shaded area marks the phase coexistence regime. Fits to $a(P)$ (dashed lines) are based on the one parameter Birch equation.

rhombohedral distortion supports the notion that the magnetic phase diagram in Fig. 2 is controlled by symmetry, rather than by chemical pressure or the effects of disorder.

Using nonresonant magnetic x-ray diffraction we searched for and found the high-pressure antiferromagnetic phase in the form of (1/2, 1/2, 1/2)-type Bragg diffraction peaks that are associated with antiferromagnetic period doubling. The longitudinal magnetic peak widths are limited by the instrument resolution as shown in Fig. 4(a), meaning that the coherence length of the antiferromagnetic domains is at least 1500 Å. This direct observation of antiferromagnetic order in compressed, stoichiometric CeFe₂, not just in its doped analogues, is essential justification for positing the generic phase diagram drawn in Fig. 2.

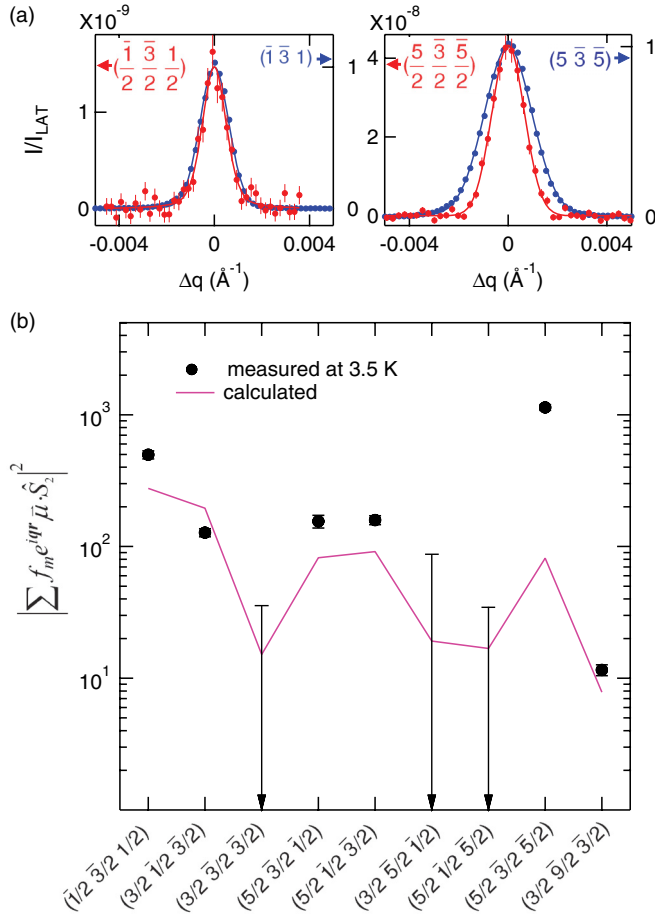


FIG. 4. (Color online) Direct observation of antiferromagnetism at $P = 3.3$ GPa and $T = 3.5$ K. (a) Longitudinal line scans of magnetic peaks (red) normalized to the lattice peaks (blue) respectively. (b) Quantity $|\sum f_m e^{iqr} \vec{\mu} \cdot \hat{S}_2|^2$ calculated using Eq. (1) for six measured diffraction peaks (black solid circles). Also shown are the sensitivity limits of null measurements at three positions (black error bars with downward arrows). Calculated values (purple line) are given for the model described in the text.

We show in Fig. 4(b) antiferromagnetic reflections at nine positions in reciprocal space, all corresponding to a single rhombohedral domain type at $P = 3.3$ GPa and $T = 3.5$ K. The nine positions yielded six measurable peaks and three null measurements, all of which can be used to constrain the magnetic structure. The orbital contributions to the magnetism in CeFe_2 are negligible compared to the spin contribution for both Ce and Fe.⁷ The nonresonant magnetic diffraction cross section is thus dominated by the projection of the spin onto the direction (\hat{S}_2) perpendicular to the scattering plane. The experimentally measured quantity is the ratio of diffraction intensity from the antiferromagnetic and the lattice Bragg peaks and is expressed as

$$\frac{I_{\text{AF}}(\frac{h}{2}, \frac{k}{2}, \frac{l}{2})}{I_{\text{LAT}}(h, k, l)} = \left(\frac{\hbar\omega}{m_e c^2} \frac{\sum f_m e^{iqr} \vec{\mu} \cdot \hat{S}_2}{8 \sum f_e e^{iqr}} \right)^2 \sin^2(2\theta). \quad (1)$$

Here (h, k, l) are Miller indices of the unit cell before antiferromagnetic period doubling. The summations in the numerator and denominator run over all scattering sites in

the magnetic and lattice unit cells, respectively, and the factor of eight in the denominator accounts for the difference in size between the magnetic and lattice unit cells. $\hbar\omega$ is the x-ray energy, 2θ is the diffraction angle of $(h/2, k/2, l/2)$, and f_m and f_e are the magnetic and atomic form factors.⁷ In Fig. 4(b), $|\sum f_m e^{iqr} \vec{\mu} \cdot \hat{S}_2|^2$ is plotted for all nine measured antiferromagnetic reflections.

V. REFINEMENT OF ANTIFERROMAGNETIC STRUCTURE

In order to constrain the magnetic structure, we resort to a general treatment of antiferromagnetic order on a face-centered lattice.^{31,32} The antiferromagnetic order doubles the unit cell along all three axes in real space. For a face-centered lattice the basis therefore increases from one to eight points, forming a bipartite lattice consisting of basis points $(1,2,3,4)$ and $(1',2',3',4')$ (Fig. 5), with the condition that the primed and unprimed points are magnetically distinguishable. There is some freedom in assigning the basis points, and in Fig. 5 we choose the assignment most natural to a structure layered along $\langle 111 \rangle$. Bear in mind that the Laves basis consists of six

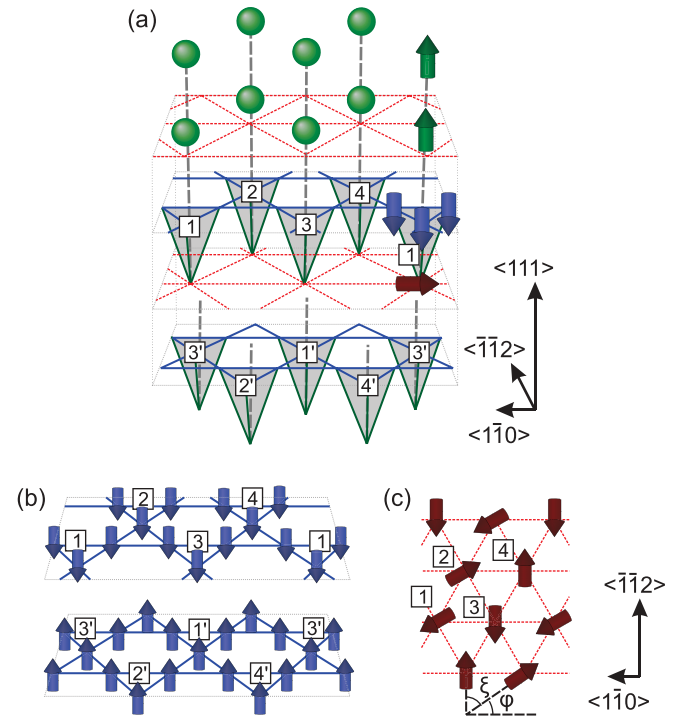


FIG. 5. (Color online) Spin structure of antiferromagnetic CeFe_2 . (a) Schematic showing the bipartite sublattice points $(1,2,3,4)$ and $(1',2',3',4')$ for a face-centered antiferromagnet.^{31,32} Each sublattice point is associated with a complete Laves basis; the Ce sites for points $1'-4'$ are omitted for clarity. The magnetic structure on site $1'$ is explicitly drawn. The spin orientations on site $1'$ are the inverse of those on site 1 , and likewise for the other pairs. (b) The kagome sheets consisting of $3e$ -Fe spins in a given sublattice are ferromagnetically aligned. (c) The $1b$ -Fe spins have an effective antiferromagnetic interaction and form a plane of frustrated triangular plaquettes. The degeneracy associated with the choice of antiferromagnetic pairs leads to a magnetic domain structure; only a single domain is drawn here for clarity.

atomic sites (four Fe and two Ce) at each point of the bipartite lattice.

The antiferromagnetic structure previously proposed for $\text{Ce}(\text{Fe}_{1-x}\text{Co}_x)_2$ on the basis of neutron and resonant x-ray diffraction measurements^{10,11} consists of ferromagnetic kagome sheets of $3e$ -Fe spins (each carrying $1.61 \mu_B$) polarized along $\langle 111 \rangle$, with the spins inverted on adjacent sheets. The Ce spins ($0.13 \mu_B$) are also parallel to $\langle 111 \rangle$ and are ordered antiferromagnetically within each $\langle 111 \rangle$ plane. The azimuthal dependence of the resonant x-ray diffraction intensity shows that the $1b$ -Fe moments ($1.12 \mu_B$) are not colinear with the $3e$ -Fe moments, and are likely polarized in the $\langle 111 \rangle$ plane.¹⁰ This is understood as the result of frustration: the $1b$ -Fe spins are ferromagnetically coupled to two oppositely polarized kagome sheets of $3e$ -Fe spins [Fig. 1(d)], and therefore are forced to lie in the $\langle 111 \rangle$ plane.

This spin structure models well the published magnetic diffraction data on $\text{Ce}(\text{Fe}_{1-x}\text{Co}_x)_2$. However, there remains ambiguity about the orientation of the $1b$ -Fe spins in the $\langle 111 \rangle$ plane^{10,11} and the related issue of magnetic domain degeneracy due to the three-fold symmetry about the $\langle 111 \rangle$ axis. The spin model proposed by Refs. 10 and 11 for $\text{Ce}(\text{Fe}_{1-x}\text{Co}_x)_2$ assumes that within each triangular lattice plane the $1b$ -Fe spins are ferromagnetically polarized along $\langle 1, -1, 0 \rangle$ and that this polarization reverses direction between subsequent triangular lattice planes along the $\langle 111 \rangle$ direction. In this model the bipartite lattice points 1–4 (Fig. 5) would have identical spin orientations, and the spins on points 1'–4' are inverted relative to those on 1–4. In addition, degenerate magnetic domains with $1b$ -Fe spins polarized along $\langle 1, 0, -1 \rangle$ and $\langle 0, 1, -1 \rangle$ should also exist as required by symmetry. It is straightforward to show that this model produces nonzero antiferromagnetic structure factors only for magnetic reflections $(h/2, k/2, l/2)$ with those odd h, k, l indices, which simultaneously satisfy the three relations $h + k, k + l, h + l = 4n + 2$.^{19,31} However, all six of the magnetic reflections that we observe at high pressure violate this selection rule. Therefore, symmetry arguments show that the published model for^{10,11} $\text{Ce}(\text{Fe}_{1-x}\text{Co}_x)_2$ is not directly transferrable to antiferromagnetic CeFe_2 at high pressure.

Nonetheless, this model can be made to agree with our data with one modification. Notice that the interaction between the $1b$ -Fe spins and their orientation within the $\langle 111 \rangle$ plane remain undetermined. If this next-nearest-neighbor interaction is antiferromagnetic, rather than ferromagnetic as assumed by Refs. 10 and 11 then the triangular plaquettes of $1b$ -Fe sites are magnetically frustrated, and the spins would be noncolinear. This introduction of nonequivalent spins on the bipartite lattice points 1–4 produces nonzero structure factors for our observed reflections.

Considering a $\langle 111 \rangle$ plane of triangular plaquettes of antiferromagnetically coupled $1b$ -Fe spins, with the magnetic moments confined to the plane by the effect of interactions with $3e$ -Fe spins, we arrive at the model shown in Fig. 5. Imposing the periodicity of the bipartite lattice basis points, and summing only over the neighboring $1b$ -Fe spin interactions, shows that the minimal semiclassical energy is obtained if the spins form antiferromagnetically aligned pairs along two independent polarization axes [such as pairs 1-2 and 3-4 in Fig. 5(c)]. The angle ξ between these two spin axes only affects the free

energy at higher order, and here we take it to be fixed at $\xi = 60^\circ$ without loss of generality.

There is degeneracy associated with the choice of these antiferromagnetically aligned pairs of $1b$ -Fe spins, giving rise to a threefold magnetic domain structure that is derived from the symmetry about the $\langle 111 \rangle$ axis. For a given domain some but not all of the reflections shown in Fig. 4(b) have nonzero structure factors. We have no knowledge of the magnetic domain population in our sample, nor of the possible variation of the angle φ between different domains. Rather than using these quantities as a source of spurious free variables, we constrain our fit of the experimental data by assuming the simplest possible domain configuration. We thus consider three equally populated domains, which differ in their values of the angle φ by 120° between domains, illustrated in Fig. 5(c). By optimizing this model to our data we determine the $1b$ -Fe moment to be $1.80 \pm 0.04 \mu_B$. The diffraction intensities calculated from this model are within a factor of two of the observed values shown in Fig. 4(b) for all but one of the measured intensities, which span over two decades in intensity. The three null measurements are also consistent with the model, which predicts diffraction intensities well below our sensitivity limits. Given the assumptions made, the quantitative agreement between predicted and observed intensities appears satisfactory. The agreement could be improved by assuming unequal magnetic domain populations and/or by optimizing the angles φ and ξ , but we feel such an analysis is unjustified given that these quantities are not independently constrained by data.

VI. COMPETING MAGNETIC INTERACTIONS AND GENERIC PHASE DIAGRAM

We are now able to draw detailed spin structures for the ferromagnetic and antiferromagnetic phases (Fig. 6). The physics underlying the generic phase diagram can be explained by considering a hierarchy of magnetic interactions between different pairs of spins, and the competition between different magnetic configurations that inevitably leave some interactions frustrated. First we point out that in both the ferromagnetic and antiferromagnetic phases, Ce possesses a nearly constant, nonvanishing moment.^{8,10,11,33} Thus the magnetism of Ce is likely to be intrinsic and not induced by the Fe moments. Furthermore, the Ce spins are always anti-aligned with the majority of the Fe spins.^{8,10,11} This suggests that an antiferromagnetic coupling (with exchange energy J_1) between the Ce and Fe spins is the dominant magnetic interaction in this system. This coupling is expected to arise from the exchange interaction between the localized Fe moments and the itinerant Ce electrons, which are hybridized from Ce $4f$ and $5d$ states. Antiferromagnetic exchange between rare-earth and transition metal ions has been reported for CeFe_2 ,⁷ Laves systems in general,^{12,34} and other intermetallic compounds.³⁵

The dominant antiferromagnetic Ce-Fe interaction determines the relatively high transition temperature for both the ferromagnetic and antiferromagnetic phases, but does not by itself determine the magnetic ground state. To understand the magnetic phase transition one has to look to the secondary magnetic interactions. The bonds between Fe nearest neighbors are ferromagnetic with exchange energy J_2 . We observe

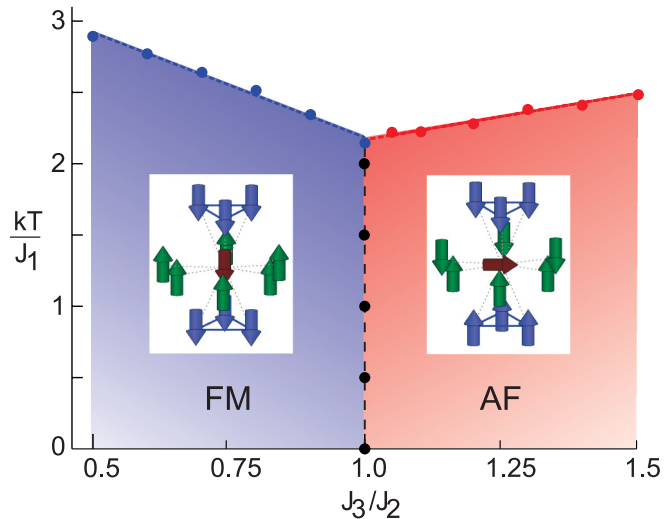


FIG. 6. (Color online) Monte Carlo simulation of the generic magnetic phase diagram. Although the energy scale is set by the strongest magnetic interaction, J_1 , the phase diagram is controlled by competition between the antiferromagnetic Ce-Ce interaction (exchange strength J_3), and the ferromagnetic Fe-Fe nearest neighbor interaction (J_2). The insets show the spin structure of CeFe_2 in both the ferromagnetic (FM) and antiferromagnetic (AF) phases for the $1b$ -Fe site and its twelve nearest neighbors. The FM spin structure is actually ferrimagnetic, as discussed in Ref. 7. In the ferromagnetic phase, the Ce-Ce bonds are frustrated, while the bonds between $1b$ -Fe and $3e$ -Fe become frustrated in the antiferromagnetic phase.

that the Ce spins are antiferromagnetically aligned in the high-pressure phase. The proximity of the magnetic phase transition in CeFe_2 to ambient pressure, and the insensitivity to the interatomic distances (Fig. 2), are strong indications that the magnetic interactions will not be *qualitatively* different on opposite sides of the transition. We therefore propose that the Ce-Ce interaction is always antiferromagnetic (with exchange energy J_3). In the ferromagnetic phase the Fe-Fe interactions are satisfied and the Ce-Ce interactions are frustrated. In the antiferromagnetic phase the Fe-Fe interactions are partially frustrated for those involving $1b$ -Fe sites, while most of the Ce-Ce interactions are satisfied. In fact, given the dominant antiferromagnetic interaction between Ce and Fe spins, it is impossible to simultaneously satisfy both the antiferromagnetic Ce-Ce and Ce-($1b$ -Fe) interactions within each triangular layer. Thus, there always exists some degree of magnetic frustration in CeFe_2 . It is the balance between the antiferromagnetic coupling of the Ce-Ce neighbors and the ferromagnetic coupling of the $1b$ -Fe to the $3e$ -Fe spins that determines the magnetic ground state. At the ferromagnetic-antiferromagnetic phase transition the effective interaction between kagome layers switches from ferromagnetic and mediated by the $1b$ -Fe spins, to antiferromagnetic and mediated by the Ce spins.

We point out that the next-nearest-neighbor interaction between $1b$ -Fe spins does not play an important role. The $1b$ -Fe spins are frustrated in the antiferromagnetic phase because of their interaction with $3e$ -Fe spins in the kagome layers. This frustration does not constrain $1b$ -Fe spins orientation within the (111) plane. Therefore, the difference in the $1b$ -Fe spin

structure between our model for CeFe_2 under pressure and the published model for^{10,11} $\text{Ce}(\text{Fe}_{1-x}\text{Co}_x)_2$ can be viewed as a relatively minor refinement due to the availability of new data. We believe that our understanding of the phase diagram as driven by competing and frustrated secondary magnetic interactions may apply to the entire family of compounds represented in Fig. 2.

To further test our proposed mechanism for arriving at a generic phase diagram, we construct a semiclassical model, taking into account only the interactions J_1 , J_2 , and J_3 (Fig. 1). We use the Hamiltonian $H = \sum J_{ij} \vec{S}_i \cdot \vec{S}_j$, where the site index $\langle i, j \rangle$ runs over all pairs of neighboring spins, both within and between unit cells, and the spins are treated as classical Ising spins. Within the mean-field approximation, minimum energy states with both ferromagnetic and antiferromagnetic arrangements can be identified. The mean-field result is confirmed by numerically examining the stability of the uniformly ordered ferromagnetic and antiferromagnetic spin structures within a classical Monte Carlo routine, which was carried out on a lattice of 288 unit cells and periodic boundary conditions, with 24 atoms per unit cell. The resulting phase diagram is shown in Fig. 6. Even at this level of approximation, the theoretical model clearly reproduces the qualitative features of the experimental phase diagram.

The generic nature of the magnetic phase diagram in Fig. 2(b) can now be understood, including the phenomenon that doped systems with both expanded and contracted lattices can be collapsed onto a single plot. The low-temperature, ambient-pressure phase of CeFe_2 is ferromagnetic, but it sits close to an antiferromagnetic phase transition and J_3/J_2 is close to the critical value. Since Al, Co, Ru, and Ir all replace Fe atoms upon being doped into CeFe_2 , they affect the Fe-Fe bonds more strongly than the Ce-Ce bonds. The dopants which end up on $1b$ -Fe sites decrease the energetic cost of the antiferromagnetic stacking of $3e$ -Fe layers and thus effectively increase J_3/J_2 . On the other hand, the application of pressure mainly affects the interatomic distances, and therefore affects both the ferromagnetic and the antiferromagnetic bonds. The latter are more sensitive to the changing overlap integrals due to the itinerant character of the Ce electrons, thus shifting J_3/J_2 towards higher values under pressure. The horizontal scaling of the different magnetic phase diagrams for chemical doping and applied pressure results from the fact that there is only a single parameter, J_3/J_2 , which controls the transition between the ferromagnetic and antiferromagnetic phases. By contrast, the thermal transition into the paramagnetic phase is controlled by J_1 , the Ce-Fe spin coupling. This strong interaction is little affected by either pressure or doping, and the vertical axes of the different phase diagrams thus line up with no additional scaling.

VII. CONCLUSION

The picture that emerges for CeFe_2 contains multiple magnetic energy scales which compete in a landscape of magnetic frustration. The dominant Ce-Fe interaction is satisfied throughout the phase diagram, and appears to be “agnostic” with respect to the ferromagnetic-antiferromagnetic transition. This primary interaction arises due to hybridization between itinerant Ce states and localized Fe $3d$ orbitals, is responsible

for the high transition temperatures of both magnetic phases in CeFe₂, and is typical of intermetallic magnets containing a rare-earth and a transition metal.^{7,12,34,35} This primary interaction sets the temperature scale for the thermal transition to long-range magnetic order, but does not select the magnetic ground state. The transition between ferromagnetism and antiferromagnetism is instead determined by the competition between the weaker, secondary interactions. If the coupling between Fe ions wins this competition then the material is a ferromagnet, and the antiferromagnetic bonds between neighboring Ce spins are frustrated. If the coupling between Ce ions wins the competition then the material is an antiferromagnet, and the frustration shifts to the Fe sublattice.

Our work underscores the value of collecting concomitant structural and magnetic information in stoichiometric materials that are free of the influence of chemical disorder. The high-pressure tuning variable provides a valuable complement to studies on chemically doped compounds, allowing us to disentangle the roles played by lattice spacing, symmetry,

disorder, frustration, and competing interactions in determining the overall phase diagram. The resulting model of frustration being shifted between sublattices may serve more generally for understanding magnetism in cubic Laves and other pyrochlore-structured intermetallic magnets.

ACKNOWLEDGMENTS

The work at the University of Chicago was supported by NSF Grant No. DMR-0907025. The work at the Advanced Photon Source and Materials Science Division of Argonne National Laboratory was supported by the US Department of Energy Basic Energy Sciences under Contract No. NE-AC02-06CH11357. P.C.C.'s work was supported by the US Department of Energy, Office of Basic Energy Science, Division of Materials Sciences and Engineering. Ames Laboratory is operated for the US Department of Energy by Iowa State University under Contract No. DE-AC02-07CH11358.

*Corresponding author: yejun@aps.anl.gov

- ¹K. Binder and A. P. Young, *Rev. Mod. Phys.* **58**, 801 (1986).
- ²J. S. Gardner, M. J. P. Gingras, and J. E. Greedan, *Rev. Mod. Phys.* **82**, 53 (2010).
- ³S. T. Bramwell and M. J. P. Gingras, *Science* **294**, 1495 (2001).
- ⁴S. Ghosh, T. F. Rosenbaum, and G. Aeppli, *Phys. Rev. Lett.* **101**, 157205 (2008).
- ⁵L. Isaev, G. Ortiz, and J. Dukelsky, *Phys. Rev. B* **79**, 024409 (2009).
- ⁶A. S. Wills *et al.*, *J. Phys.: Condens. Matter* **18**, L37 (2006).
- ⁷O. Eriksson, L. Nordström, M. S. S. Brooks, and B. Johansson, *Phys. Rev. Lett.* **60**, 2523 (1988).
- ⁸S. J. Kennedy, P. J. Brown, and B. R. Coles, *J. Phys.: Condens. Matter* **5**, 5169 (1993).
- ⁹L. Paolasini *et al.*, *Phys. Rev. B* **58**, 12117 (1998).
- ¹⁰L. Paolasini *et al.*, *Phys. Rev. Lett.* **90**, 057201 (2003).
- ¹¹L. Paolasini *et al.*, *Phys. Rev. B* **77**, 094433 (2008).
- ¹²P. J. Brown *et al.*, *J. Phys.: Condens. Matter* **4**, 1103 (1992).
- ¹³R. Ballou, E. Lelièvre-Berna, and B. Fåk, *Phys. Rev. Lett.* **76**, 2125 (1996).
- ¹⁴I. Mirebeau, I. N. Goncharenko, and I. V. Golosovsky, *Phys. Rev. B* **64**, 140401 (2001).
- ¹⁵D. F. Franceschini and S. F. da Cunha, *J. Magn. Magn. Mater.* **51**, 280 (1985).
- ¹⁶Y. Nishihara, *J. Magn. Magn. Mater.* **70**, 75 (1987).
- ¹⁷S. J. Kennedy, A. P. Murani, B. R. Coles, and O. Moze, *J. Phys. F* **18**, 2499 (1988).
- ¹⁸S. B. Roy and B. R. Coles, *Phys. Rev. B* **39**, 9360 (1989).
- ¹⁹S. J. Kennedy and B. R. Coles, *J. Phys. Condens. Matter* **2**, 1213 (1990).
- ²⁰A. K. Rajarajan, S. B. Roy, and P. Chaddah, *Phys. Rev. B* **56**, 7808 (1997).
- ²¹H. Fukuda, H. Fujii, H. Kamura, Y. Hasegawa, T. Ekino, N. Kikugawa, T. Suzuki, and T. Fujita, *Phys. Rev. B* **63**, 054405 (2001).
- ²²H. Okada *et al.*, *J. Phys. Soc. Jpn.* **73**, 1982 (2004).
- ²³J. P. Sanchez, P. Vulliet, and M. M. Abd-Elmeguid, *Hyperfine Interact.* **133**, 5 (2001).
- ²⁴T. Fujiwara *et al.*, *Physica B* **312-313**, 336 (2002).
- ²⁵D. Braithwaite *et al.*, *Phys. Rev. B* **76**, 224427 (2007).
- ²⁶K. A. Gschneidner and V. K. Pecharsky, *Z. Kristallogr.* **221**, 375 (2006).
- ²⁷L. Braicovich *et al.*, *Phys. Rev. B* **56**, 15047 (1997).
- ²⁸P. C. Canfield and I. R. Fisher, *J. Cryst. Growth* **225**, 155 (2001).
- ²⁹Y. Feng *et al.*, *Phys. Rev. Lett.* **99**, 137201 (2007).
- ³⁰Y. Feng, R. Jaramillo, J. Wang, Y. Ren, and T. F. Rosenbaum, *Rev. Sci. Instrum.* **81**, 041301 (2010).
- ³¹W. L. Roth, *Phys. Rev.* **110**, 1333 (1958).
- ³²W. L. Roth, *Phys. Rev.* **111**, 772 (1958).
- ³³A. Delobbe *et al.*, *Euro. Phys. Lett.* **43**, 320 (1998).
- ³⁴H. Yamada and M. Shimizu, *J. Phys. F* **16**, 1039 (1986).
- ³⁵B. Szpunar, *Physica B* **130**, 29 (1985).